Molecular dynamics simulations of sodium nanoparticle deposition on magnesium oxide

Yannick Fortouna[1,4], Pablo de Vera[1,2,*] Alexey V. Verkhovtsev[1,3], and Andrey V. Solov'yov[1,3]
[1] *MBN Research Center, Altenhöferallee 3, 60438 Frankfurt am Main, Germany*
[2] *Departamento de Física–Centro de Investigación en Óptica y Nanofísica, Regional Campus of International Excellence "Campus Mare Nostrum", Universidad de Murcia, 30100 Murcia, Spain*
[3] *On leave from A.F. Ioffe Physical-Technical Institute, Polytekhnicheskaya 26, 194021 St. Petersburg, Russia and*
[4] *Currently at Department of Materials Science and Engineering, University of Ioannina, 45110 Ioannina, Greece*
(Dated: July 7, 2021)

ABSTRACT:
The interaction of mass-selected atomic clusters and nanoparticles with surfaces attracts strong interest in view of fundamental research and technological applications. Understanding dynamics of the deposition process is important for controlling structure and functioning of deposited nanoparticles on a substrate, but experimental techniques can usually observe only the final outcome of the deposition process. In this paper, the deposition of 4 nm-sized sodium nanoparticles on an experimentally relevant magnesium oxide substrate is studied by means of classical molecular dynamics simulations. An empirical force field is derived which accounts for the interaction of highly polarizable Na atoms with the surface, reproducing the results of previously reported quantum mechanics/molecular mechanics simulations. Molecular dynamics simulations permit exploring the dynamics of deposited nanoparticles on long timescales on the order of hundreds of picoseconds, thus enabling the analysis of energy relaxation mechanisms and the evolution of nanoparticle structure up to its thermalization with the substrate. Several nanoparticle characteristics, such as internal structure, contact angle, and aspect ratio are studied in a broad deposition energy range from the soft landing to multi-fragmentation regimes.

Keywords: Sodium nanoparticle; magnesium oxide; nanoparticle deposition process; molecular dynamics

I. INTRODUCTION

Metal clusters, nanoparticles and nanoalloys have been a subject of intense research over the past decades [1–8]. Unique and size-dependent structural, electronic, optical and magnetic properties of these systems have led to various technological applications. For instance, metal clusters and nanoparticles, both monatomic and bimetallic, can be used as junctions in nanoelectronic devices [9] or as elements of photonic crystals [10]. They are also useful for energy, environmental and medical applications, e.g. as catalysts [11], contrast agents in medical imaging [12], and radiosensitizers in cancer treatment with ionizing radiation [13–15].

Many of these applications involve the interaction of clusters with molecular environments or with surfaces which serve as a support [4]. Understanding the dynamics of cluster deposition is of high relevance for controlling the structure and properties of supported clusters. Depending on deposition conditions, structure of clusters on the substrate can be either preserved or changed substantially, or clusters may experience fragmentation including possible penetration into the substrate and/or modification of the latter [16–20]. The ability to control these processes lays in the core of key experimental techniques for the fabrication of thin films and nanodevices, such as cluster ion beam assisted deposition, sputtering, surface smoothing or substrate implantation [21, 22].

The shape of clusters and nanoparticles on a surface is determined by the interplay of different processes and phenomena, including electron shell closure [23–25], interaction of deposited systems with the substrate [26, 27], relaxation of thermal energy remaining after the collision by means of heat transfer, and atomic rearrangements caused by collision-induced mechanical stress or phase transitions [5, 6]. These processes depend on the type and temperature of the substrate, the size and composition of the deposited cluster/nanoparticle and on the deposition energy. For small atomic clusters containing $N \lesssim 200$ atoms quantum effects, such as even-odd oscillations in cluster abundance spectra and the appearance of "magic" numbers associated with electron shell closure, play a crucial role in determining the shape of clusters on a surface [24]. However, these effects shrink with increasing the system size up to $N \sim 10^3$ [6]. While clusters made up of a few atoms usually keep their structure upon soft landing (i.e. when kinetic energy per atom is much smaller than the cluster cohesion energy) [28, 29], large clusters and nanoparticles can experience significant deformations, such as flattening, surface wetting or epitaxial alignment [21, 30–32]. Hard deposition at kinetic energies exceeding the cohesion energy can lead to cluster fragmentation.

The deposition of metal clusters and nanoparticles on various surfaces has been widely studied experimentally

* pablo.vera@um.es

(see e.g. Ref. [21] and references therein). However, experimental studies are usually limited to the observation of the final state of the deposition process, and the study of the cluster deposition mechanisms thus commonly relies on theoretical methods [21, 33–35]. For instance, detailed quantum mechanics/molecular mechanics (QM/MM) simulations of the deposition of small sodium clusters on magnesium oxide substrates were reported in Refs. [29, 35–37]. These materials were selected to highlight the importance of both electron and nuclear dynamics in the process of cluster deposition. Sodium is a highly polarizable metal having a single valence electron. Magnesium oxide is a hard ionic crystal with a highly corrugated potential energy surface which can easily polarize Na atoms and produce complex interaction patterns.

The study of metallic aggregates deposited onto oxide surfaces is important for technological applications, especially in the field of catalysis [38]. Deposition, dynamics and diffusion of metal clusters on MgO films has particularly attracted both experimental and theoretical interest [38–40], including a number of recent studies [41–44].

QM/MM simulations conducted in Refs. [29, 35–37] explored different deposition regimes for small Na_6 and Na_8 clusters including soft landing, hard collision and reflection of the clusters. Structure and dynamics of the clusters as well as the mechanisms of energy transfer to the substrate were analyzed in detail. However, due to the complexity and computational cost of QM/MM calculations, this analysis could only be carried out for very small clusters, short simulation times (on the order of several picoseconds) and zero temperature.

Contrary to *ab initio* approaches, classical molecular dynamics (MD) permits simulating deposition of much bigger systems at finite temperature and over significantly longer timescales, thus allowing to explicitly account for the process of energy relaxation [17–20, 27, 31, 45–48]. Empirical force fields employed in MD simulations can be tuned to effectively reproduce the collision dynamics observed in QM/MM calculations on much shorter time scales.

This paper reports a detailed theoretical analysis of the deposition of Na_{1067} nanoparticles ($\sim$ 4 nm in diameter) on a MgO (001) substrate. The simulations are conducted for a wide deposition energy range (from the soft-landing to nanoparticle multifragmentation regimes) and at several finite temperatures at which the nanoparticle is either in the solid state or in the form of a liquid droplet. A force field describing the interaction of Na atoms with the MgO surface is developed and used in the simulations. The force field reproduces main features of the deposition of a single Na atom, obtained previously in QM/MM simulations [29]. The MD technique has been employed to simulate deposition and post-collision dynamics of the nanometer-sized sodium nanoparticles. Several aspects of the deposition process are explored as a function of deposition energy, including the change of the nanoparticle structure and shape (i.e., the nanoparticle aspect ratio), its wetting properties (through the analysis of the contact angle), as well as the energy transfer between the nanoparticle and the substrate, leading to the thermalization of the energy of the excited nanoparticle with the substrate.

This study provides detailed atomistic insights into the dynamics of sodium nanoparticle deposition on magnesium oxide substrates, which complement the information already gathered for small clusters from QM/MM simulations and which may be useful for experimental studies. The analysis, focusing on the quantification of final aspect ratios and contact angles as a function of deposition energy in a wide energy range, brings about detailed information which is not always available in the literature.

II. COMPUTATIONAL METHODOLOGY

In the performed classical MD simulations the coupled Langevin equations for all atoms in the system are solved numerically by means of the leapfrog algorithm [49]. Simulations of the deposition of a 4 nm diameter sodium nanoparticle on MgO(001) surface have been performed for systems pre-equilibrated at 77 K and 300 K. These temperatures allow the comparison of the deposition dynamics for a solid nanoparticle and a liquid droplet, having into account that the melting temperature of Na_{1067} is slightly below 300 K [50].

All simulations have been performed by means of MBN Explorer [51], the software package for advanced multiscale modeling of complex molecular structure and dynamics [49]. The MgO substrate and the sodium nanoparticle are constructed by means of the dedicated multi-task toolkit MBN Studio [52]. This software has also been used to prepare all other necessary input files and to analyze simulation results. In the following sections, the construction and preparation of each part of the system is described, together with the potential used for each interatomic interaction.

A. Magnesium oxide substrate

The interactions involving Mg and O atoms are described based on the nuclear contribution to the empirical potential which was defined in earlier QM/MM calculations [29, 35]. Details of this potential, being a combination of exponential and power potentials, as well as its parameters can be found in Table 4 of Ref. [35]. All atoms in the substrate carry partial charges of $\pm 2|e|$ (with e being the elementary charge) and thus interact also through the Coulomb potential. The electrostatic interactions are treated by means of the Ewald algorithm implemented in MBN Explorer [49].

A face-centered cubic structure of MgO with a lattice parameter of 4.212 Å has been employed to create substrates with the size of 12.21×12.21 nm^2 and

24.43×24.43 nm^2 in the x-y directions, simulated using periodic boundary conditions. Following Ref. [53] the substrate is formed by seven atomic layers in the z-direction normal to the surface. The height of the constructed substrate (12.6 Å) exceeds significantly the range of Na–Mg and Na–O interatomic interactions (see Section II B below). For creating the substrate, one should keep in mind that energetic cluster collisions can build up a strong pressure wave in the form of a shock wave propagating through the substrate [17, 18]. When this happens, specially designed boundary conditions are needed to avoid the reflection of the shock wave into the simulation box, which could produce artefacts in the trajectories [54]. However, it has been checked that, for the deposition energies considered in this study, only small-amplitude oscillations are produced for the substrate atoms, and no significant pressure wave appears that prevents the need to use such absorbing boundary conditions.

The structure of MgO has been optimized using the velocity quenching algorithm and the time step of 0.1 fs. After structure optimization the substrate is equilibrated using the Langevin thermostat with a damping time of 0.1 ps to the target temperatures of 77 K and 300 K such that obtained atomic velocities correspond to the Maxwell-Boltzmann distribution.

B. Sodium atom–substrate interaction

The interaction between Na and O or Mg atoms is described by means of the following pairwise potential:

$$U_{ij}(r) = D_{ij}\left[e^{-2\beta_{ij}\,(r\,-\,r_{0,ij})} - 2e^{-\beta_{ij}\,(r\,-\,r_{0,ij})}\right] - \frac{C_i}{r^4} + \frac{q_i q_j}{\varepsilon_0 r}\,, \qquad (1)$$

where r is the distance between atoms i and j. The first term on the r.h.s. of Eq. (1) describes a Morse-type interaction, whereas the second and third terms describe the long-range polarization and electrostatic interactions, respectively. Parameters D_{ij}, $r_{0,ij}$ and β_{ij} of the Morse potential represent the depth of the potential well, equilibrium interatomic distance and steepness of the potential for each pair of atoms. q_i and q_j are atomic partial charges, ε_0 is the effective charge screening factor (set equal to 1 in present simulations), and C_i is an empirical parameter determining the intensity of the polarization forces for the interaction of Na with a particular atom i. The long-range Coulomb interaction is calculated by means of the Ewald algorithm [49]. The partial charge $q_{\rm Na}$ on the Na atom is treated as a variable parameter to account for additional attracting forces between the atom and the surface due to its strong polarizability in the field of the ionic crystal.

The parameters for the potential (1) have been obtained by a trial and error procedure in an iterative manner until a reasonable agreement with reference data from QM/MM simulations [29, 35] has been reached. In particular, the adsorption energy and dynamics of a single Na atom on top of Mg and O sites on the surface of MgO have been evaluated and compared with the reference *ab initio* calculations [29, 35]. The best agreement in terms of both energetics and dynamics of a sodium atom atop MgO is achieved with the parameters summarized in Table I. The resulting adsorption energy curves for a Na atom on top of Mg and O sites are shown in Fig. 1. A partial charge $q_{\rm Na} = +0.29|e|$ has been assigned to the Na atom in this case. Note that when the Na–O and Na–Mg interactions are described only with the Morse potential or when the partial charge on a sodium atom is set equal to zero, simulated MD trajectories deviate from the earlier QM/MM results, which can be attributed to underestimation of the attractive forces. The calculated adsorption energies reproduce the shape of the QM/MM results, presenting only slightly deeper potential wells. It should be noted that variation on the order of a few tenths of eV can arise by considering different exchange-correlation functionals and basis sets in quantum chemistry calculations. We have ensured that the derived empirical potential, Eq. (1), provides a reasonable agreement with the dynamics of a single Na atom on MgO and gives results consistent with QM/MM simulations of Na_6 and Na_8 cluster deposition [29]. The constructed potential is thus deemed suitable for the simulation of the

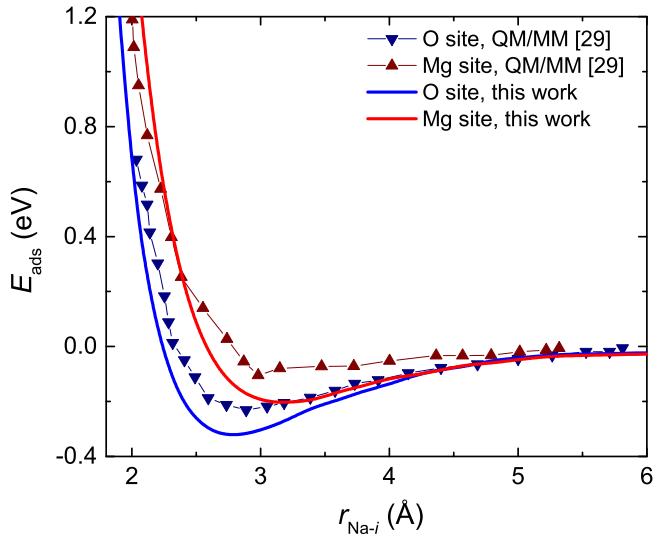

FIG. 1. Adsorption energy of a Na atom on the MgO surface as a function of the distance between Na and O or Mg sites. Present MD empirical force field calculations (lines) are compared to QM/MM results (symbols) [29].

TABLE I. Parameters of the force field for Na–O and Na–Mg interactions, Eq. (1), used in the simulations.

Atom pair	D_{ij} (eV)	β_{ij} (Å^{-1})	$r_{0,ij}$ (Å)	C_i (eV Å^4)
Na–O	0.099	1.5	2.94	0.5
Na–Mg	0.001	1.32	4.85	0.5

deposition of a nanometer-sized sodium nanoparticle.

C. Sodium nanoparticle

A spherical sodium nanoparticle of 4 nm diameter, containing 1067 atoms, is cut out from the corresponding bulk crystal by means of MBN Studio [52]. Geometry of the nanoparticle has been optimized first using the velocity quenching algorithm with a 0.1 fs time step. The many-body Gupta potential is used to describe the interatomic interactions with parameters taken from Ref. [55].

After initial energy minimization the nanoparticle has been annealed to create a more energetically favorable starting geometry for the deposition simulations. Several annealing cycles have been simulated following the procedure reported in Ref. [56]. The first cycle consists of heating from 0 K to 400 K at a rate of 0.08 K/ps, followed by a constant temperature simulation at 400 K for 2 ns, and cooling down to 0 K at a rate of 0.08 K/ps. The follow-up cycles are similar but the nanoparticle has been heated up to 200 K, a temperature slightly below the cluster melting temperature, to allow surface reorganization without complete melting of the nanoparticle. The nanoparticle melting temperature of 260 K is determined by simulating heating of the annealed structure. The evaluated melting temperature of the nanoparticle is close to the experimentally determined values of $280 - 290$ K [50]. Cohesive energy of the nanoparticle converges to 1.0194 eV/atom after three annealing cycles. A nearly icosahedral shape has been obtained (see Fig. 2(a)), comprising a mix of face centered cubic and hexagonal compact structures. It is well known that the icosahedron is a particularly stable configuration for clusters of sodium and other elements in a broad size range [50, 55, 57, 58], so the obtained structure is reasonable. In any case, the energy difference between different nanoparticle isomers is typically in the meV range, so the initial structure should not affect much the process of nanoparticle deposition. The nanoparticle has been equilibrated to the target temperatures of 77 K and 300 K by means of the Langevin thermostat, and the resulting velocities correspond to the Maxwell-Boltzmann distribution.

D. Deposition simulations

MD simulations of the nanoparticle deposition on the substrate have been performed in the NVE microcanonical ensemble, thus ensuring conservation of the total energy of the system. The nanoparticle is placed in the center of the simulation box at a 10 Å distance from the surface, such that initial nanoparticle-substrate interactions are negligible (see Fig. 1). Initial atomic velocities are taken from pre-equilibration simulations at 77 K and 300 K in order to simulate the deposition process at low temperature at which the nanoparticle is solid, as well as at room temperature at which the nanoparticle has the shape of a liquid droplet. The partial charge of $+0.29|e|$, derived in the fitting procedure described in Section II B, is equally distributed among all the atoms in the nanoparticle. Additional velocities in the direction normal to the surface are given to every atom of the nanoparticle such that the nanoparticle is deposited with kinetic energies $E_{\rm dep}$ = 0.0034, 0.0068, 0.0136, 0.034, 0.068, 0.102, 0.136, 0.34, 0.68 and 1.36 eV/atom. The initial configuration of the system is illustrated in Fig. 2(a).

Note that cluster collision-induced shock waves in the substrate are typically observed for impact energies ≥ 10 eV/atom, but not for the energies of 1 eV/atom or lower [17]. Only small-amplitude oscillations of the substrate atoms have been observed for the studied impact energies. Therefore no special pressure-absorbing boundary conditions [54] have been used. Similarly, the heat transfer during deposition can change the substrate temperature, which may lead to the necessity of suitable thermostats to remove the excess kinetic energy in the system boundaries. It has been checked that the constructed substrate has enough atoms to effectively damp the temperature spike after the collision. An increase of the average substrate temperature by several kelvins has been observed for the larger impact energies, that is negligibly small as compared to the temperature increase in the nanoparticle (see Section III B).

A 12.21×12.21 nm^2 substrate has been used for most simulations. However, a larger substrate of 24.43×24.43 nm^2 has been employed for deposition energies larger than 0.34 eV/atom to avoid interaction of the heavily deformed or fragmented nanoparticle with its periodic images. Two bottom MgO layers are fixed to avoid the displacement of the substrate upon nanoparticle impact. Simulations have been performed using the leapfrog algorithm with a 1 fs time step, which ensures that variation of the total energy does not exceed 0.1%. As described in Section III, most of the phenomena arising during deposition have been observed within the first 50 ps of the simulations. Nonetheless, longer simulations up to 500 ps have been conducted in some cases to analyze the dynamics of the system on the longer time scale.

III. RESULTS AND DISCUSSION

In Section III A we briefly discuss the time evolution of the shape and structure of the nanoparticle at different deposition energies. Then, in Section III B we analyze how fast the nanoparticle has reached thermal equilibrium with the substrate after the deposition. In Section III C we quantitatively characterize the final shape acquired by the nanoparticle at different deposition energies and evaluate the contact angle with the substrate. Finally, the longer-term changes of the internal structure of the nanoparticle are analyzed in Section III D.

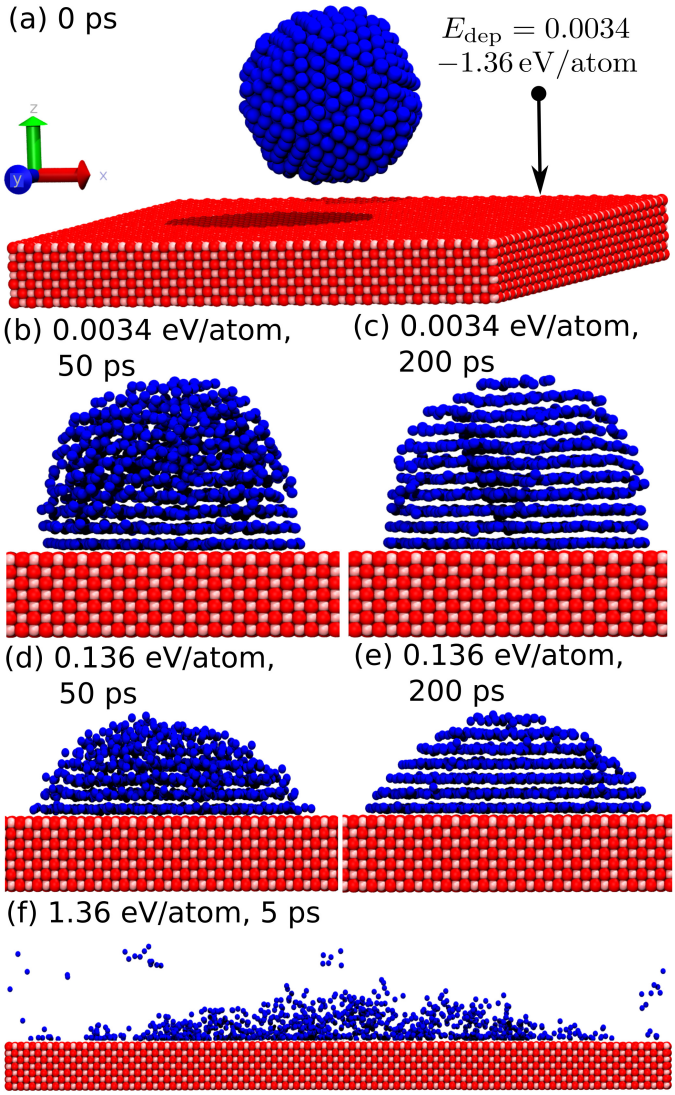

FIG. 2. MD snapshots of the Na_{1067} nanoparticle deposited on a MgO substrate at several deposition energies. Panel (a) shows the initial geometry of the system. Panels (b-f) illustrate three different deposition regimes, see text for details: (b)-(c) nanoparticle structure after 50 and 200 ps, respectively, for $E_{dep} = 0.0034$ eV/atom; (d)-(e) the same as previous for $E_{dep} = 0.136$ eV/atom; (f) snapshot of the fragmented nanoparticle deposited at $E_{dep} = 1.36$ eV/atom after 5 ps.

A. Shape and structure of the deposited nanoparticle

Figure 2 presents several MD snapshots of the Na_{1067} nanoparticle (pre-equilibrated at 77 K) deposited on MgO at different deposition energies E_{dep}. Three distinct deposition regimes have been observed as shown in Fig. 2(b-f). In the "soft" collision regime (e.g. at $E_{dep} =$ 0.0034 eV/atom, see panels (b) and (c)) the nanoparticle remains in the solid phase in the course of deposition. At more energetic collisions (e.g. at $E_{dep} = 0.136$ eV/atom, see panels (d) and (e)) the nanoparticle undergoes a collision-induced melting phase transition followed by its subsequent re-crystallization. Finally, the "hard" collision regime (e.g. at $E_{dep} = 1.36$ eV/atom, panel (f)) leads to rapid multifragmentation of the nanoparticle. A detailed analysis of the nanoparticle shape is presented below in Section III C.

Figures 2(b-e) show snapshots from the simulations taken at time instances of 50 ps and 200 ps. The nanoparticle shape is stabilized by about 50 ps and does not change significantly at larger simulation times. The nanoparticle deposited at $E_{dep} = 0.0034$ eV/atom acquires the shape of a truncated prolate spheroid, see panels (b) and (c). Deposition at the 40 times larger energy results in the formation of a truncated oblate spheroid as shown in panels (d) and (e). Note that some sodium atoms arrange into layers parallel to the MgO surface as a result of the nanoparticle-substrate interaction. The formation of two sodium layers is clearly seen after the first 50 ps of the simulations while the whole nanoparticle acquires a layered structure after 200 ps. This behavior is similar to the well-known phenomenon of epitaxial alignment which has been studied both experimentally and computationally [21]. Finally, Fig. 2(f) illustrates the case of "hard" deposition leading to rapid fragmentation of the nanoparticle. At deposition energy of 1.36 eV/atom (which exceeds the calculated cohesive energy of the nanoparticle, 1.019 eV/atom) multifragmentation of Na_{1067} and the formation of sodium atoms and small sodium clusters is observed within the first 5 ps of the simulation.

For large impact energies, shock waves can be formed in the substrate [17, 18], which should be treated by means of pressure-absorbing boundary conditions [54]. This effect was observed in Ref. [17] for Mo clusters deposited on a Mo substrate at impact energies ≥ 10 eV/atom, i.e. at much larger energies than the ones studied here. Pressure waves have not been observed in the simulated trajectories, which justifies the use of the relatively small substrate employed in this work. In any case, the results for the larger impact energies which lead to fission or multifragmentation of the nanoparticle (see Section III B) should be taken as qualitative.

B. Thermalization of the nanoparticle on the surface

Figure 3 illustrates how instantaneous temperature of the nanoparticle and the substrate evolves in the course of simulations. Results shown in panels (a) and (b) are obtained for the nanoparticle pre-equilibrated at 77 K and deposited at $E_{dep} = 0.0068$ eV/atom and 0.068 eV/atom, respectively. As shown in Figure 3, the nanoparticle reaches thermal equilibrium with the substrate at time instances of about 400–500 ps. Before thermalization, temperature of the nanoparticle exhibits a similar behavior in the two cases considered: it first increases rapidly as the nanoparticle hits the surface and

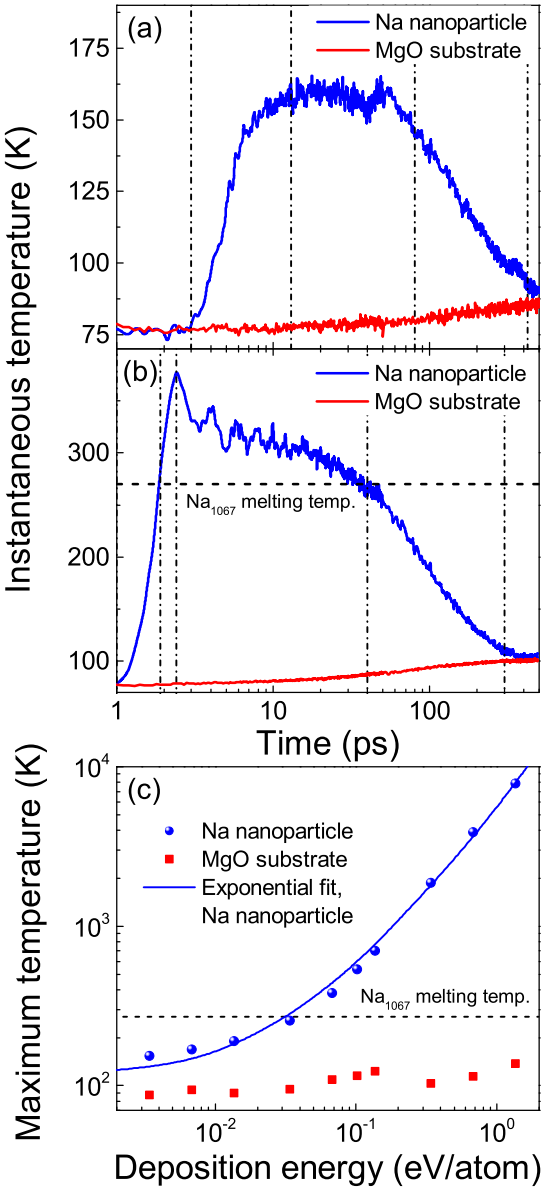

FIG. 3. Instantaneous temperature of the Na_{1067} nanoparticle and the MgO substrate as a function of simulation time for deposition energies of (a) 0.0068 eV/atom and (b) 0.068 eV/atom. Panel (c) shows maximum instantaneous temperature of the nanoparticle and the substrate as a function of deposition energy.

then it decreases gradually while the nanoparticle transfers its energy to the substrate. It is important to note here that simulations have been conducted in the NVE ensemble and for the substrate of reduced dimensions, and that no thermostat has been used to simulate the heat transfer to a semi-infinite substrate [54]. The absence of a thermostat causes a small increase of the substrate temperature (by a few tens of degrees) which will disappear if one would apply a thermostat. However, the substrate temperature increase is very small in comparison with the temperature acquired by the nanoparticle.

TABLE II. Parameters for the fitting functions, Eqs. (2), (8) and (9), describing the maximum instantaneous temperature of the sodium nanoparticle after deposition, the nanoparticle aspect ratio, and the contact angle between the nanoparticle and the substrate at the end of simulations, respectively.

T_0 (K)	−16640.6
T_1 (K)	16754.7
ω (eV^{-1}/atom)	0.28
δ_0	3.52
δ_1	−2.18
α (eV^{-1}/atom)	16.62
θ_0 (deg.)	68.59
θ_1 (deg.)	23.61
γ (eV^{-1}/atom)	33.92

Therefore, the heat transfer scenario will not change significantly with the introduction of a thermostat.

Figure 3(c) shows the maximum temperature of the nanoparticle and the substrate, reached after the first 50 ps of the simulation, for different deposition energies considered in this study. As commented above, the small increase of the substrate temperature should not be considered as an exact result, as it is due to the absence of a thermostat when simulating the semi-infinite material. However, the observed increase is negligible in comparison with that in the nanoparticle. The calculated dependence of the maximal nanoparticle temperature $T_{\max}$ on $E_{\rm dep}$ has been fitted with an exponential function:

$$T_{\max} = T_0 + T_1\, e^{\omega\, E_{\rm dep}}\ , \qquad (2)$$

where T_0, T_1 and ω are the fitting parameters listed in Table II. The exponential fitting does not bear any physical meaning, but is used as a convenient parametrization of the results.

Dashed horizontal lines in Fig. 3(b-c) illustrate the melting temperature of Na_{1067} obtained from simulations, $T_{\rm m} \approx 260$ K. Temperature of the nanoparticle deposited at $E_{\rm dep} = 0.0068$ eV/atom does not exceed that threshold value during the whole simulation (see Fig. 3(a)), indicating that the nanoparticle remains in the solid phase during deposition. In contrast, instantaneous temperature of the nanoparticle deposited at 0.068 eV/atom exceeds the melting temperature after the first few picoseconds, see Fig. 3(b). The temperature reaches the maximal value of about 380 K and remains larger than the melting temperature of the nanoparticle for several tens of picoseconds, until it drops below the threshold value, gradually approaching thermal equilibrium with the substrate at time instances of about 400 ps.

Two regimes which do not lead to nanoparticle fragmentation have thus been identified in the simulations. Figure 3(c) shows that at deposition energies below 0.034 eV/atom the nanoparticle remains in the solid phase throughout the whole simulation. At larger values of $E_{\rm dep}$ the instantaneous temperature of the nanoparticle exceeds the melting temperature so that the nanoparticle has experienced the melting phase transition fol-

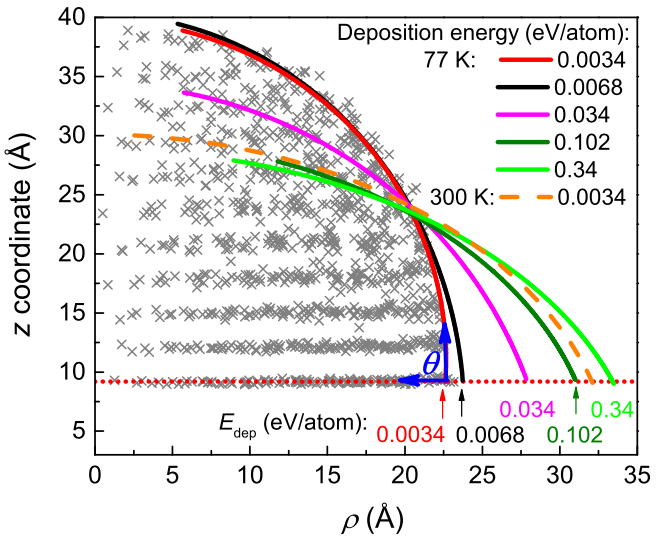

FIG. 4. Radial profile of the Na_{1067} nanoparticle deposited on MgO. Symbols show the distribution of sodium atoms of the nanoparticle pre-equilibrated at 77 K and deposited at E_{dep} = 0.0034 eV/atom, after 50 ps of the simulation. Colored curves depict radial profiles of the nanoparticle deposited at different E_{dep}, obtained by means of Eq. (4).

lowed by re-crystallization. Deposition at energies above 0.68 eV/atom has led to fission or multifragmentation of the nanoparticle.

C. Contact angle and aspect ratio of the nanoparticle

Coordinates of sodium atoms extracted from each simulated MD trajectory are used to parameterize the shape of the deposited nanoparticle.

As follows from the simulated trajectories, the sodium nanoparticle is, to a good approximation, radially symmetric with respect to the main axis z. In order to characterize the shape of the nanoparticle, cylindrical coordinates (ρ, z) are introduced, where:

$$\rho = \sqrt{(x - x_{CM})^2 + (y - y_{CM})^2} \ , \qquad (3)$$

with x_{CM} and y_{CM} being x- and y-projections of the center of mass of the nanoparticle. The ρ-axis lies in the MgO surface plane, whereas z-axis is perpendicular to the surface.

Figure 4 shows by symbols (z, ρ) projections of atoms in the Na_{1067} nanoparticle deposited at 77 K with an energy of 0.0034 eV/atom. The shown distribution of atoms is evaluated at the 50 ps time instance by which the shape of the deposited nanoparticle has been stabilized. The horizontal dotted line of ordinate $z_0 \approx 9$ Å depicts average positions of sodium atoms in the bottom-most atomic layer of the nanoparticle, which is closest to the MgO surface.

In order to evaluate the contact angle between the nanoparticle and the substrate, we have selected coordinates of atoms located on the nanoparticle's surface and fitted the resulting set of coordinates with the following equation [27, 59, 60]:

$$\rho(z) = \sqrt{a\,(z - z_0)^2 + b\,(z - z_0) + c} \quad , \quad z \geq z_0 \ , \qquad (4)$$

where a, b and c are fitting parameters. Solid colored curves in Fig. 4 show the inverse dependence $z(\rho)$ for the Na_{1067} nanoparticle equilibrated at 77 K and deposited at different energies as indicated by labels. From this dependence the nanoparticle contact angle θ is determined as [59]:

$$\theta = \arctan\left(\left. \frac{dz}{d\rho} \right|_{\rho=\rho'} \right) \ , \qquad (5)$$

where ρ' is the point of intersection between the fitting curve and the line $z = z_0$ representing the bottom-most Na atomic layer parallel to the substrate surface.

Solid curves shown in Fig. 4 illustrate a gradual change of the nanoparticle shape from a truncated prolate spheroid ($z_{max} > \rho_{max}$) to a semi-spheroid ($z_{max} = \rho_{max}$) to a truncated oblate spheroid ($z_{max} < \rho_{max}$) as the deposition energy increases. The dashed orange curve in Fig. 4 shows the $z(\rho)$ dependence for the nanoparticle equilibrated at 300 K and deposited at E_{dep} = 0.0034 eV/atom. It is apparent that the nanoparticle equilibrated at room temperature acquires a droplet-like oblate shape on the surface even at the lowest energy considered. These results agree with the simulation snapshots shown in Fig. 2(b-e).

Note that the shape of the Na_{1067} nanoparticle equilibrated at 77 K and deposited at 0.34 eV/atom (light green curve) is very similar to that of the nanoparticle equilibrated at 300 K and deposited at much lower energy of 0.0034 eV/atom (dashed orange curve). In the former case the nanoparticle has experienced a collision-induced melting phase transition while in the latter case it has been directly deposited as a liquid droplet. The equilibrium shape of the nanoparticle deposited at 300 K depends very little on deposition energy. As a result, the shapes of the nanoparticles deposited at higher values of E_{dep} (below the threshold energy for nanoparticle fragmentation) are similar to the one shown for E_{dep} = 0.0034 eV/atom (see the dashed orange curve). Dependence of the contact angle on E_{dep} is discussed in greater detail below.

We have also analyzed the ratio of the diameter of the bottom-most atomic layer of the nanoparticle (see red dotted line in Fig. 4) to the nanoparticle height, i.e. the nanoparticle aspect ratio [21]. It is defined as

$$\delta = \frac{2\rho(z_0)}{z(\rho = 0)} \ . \qquad (6)$$

The temporal evolution of δ for the nanoparticle deposited at different energies is illustrated in Fig. 5. Panels (a) and (b) illustrate the deposition at 77 K and

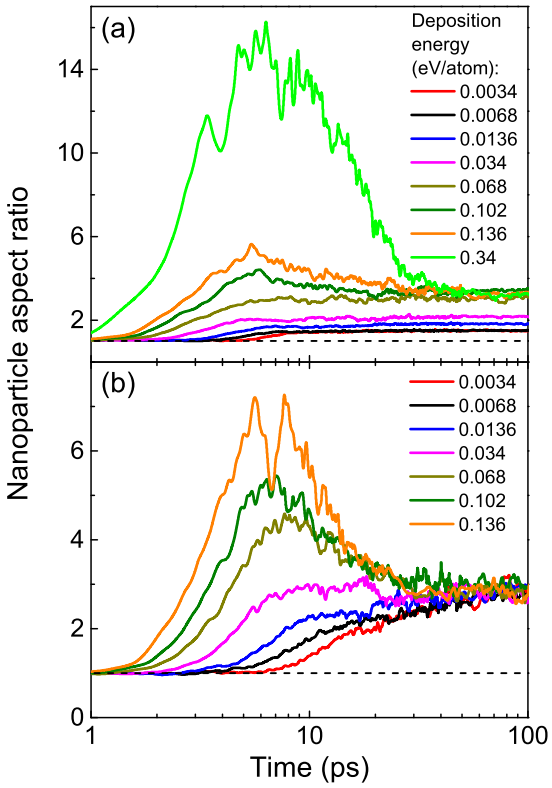

FIG. 5. Nanoparticle aspect ratio δ, Eq. (6), as a function of simulation time for deposition at (a) 77 K and (b) 300 K.

300 K, respectively. We consider here the values of $E_{\rm dep}$ up to 0.34 eV/atom for 77 K and up to 0.136 eV/atom for 300 K, which are energy values at which the nanoparticle have not fragmented upon collision with the substrate. Values of δ between 1 and 2 indicate that the nanoparticle acquires the shape of a truncated prolate spheroid, whereas $\delta = 2$ describes a perfect semi-spheroid. A parallel can be drawn with the snapshots of nanoparticle deposition at 77 K, shown in Fig. 2(b-e). As discussed above, the overall shape of the nanoparticle practically does not change after 50 ps of simulation. This observation is confirmed by constant values of δ observed after 50 ps. As shown in Fig. 5 this trend has been observed for all deposition energies within the range considered.

Three distinct deformation regimes have been revealed by analyzing the final aspect ratios. At very low deposition energies ($E_{\rm dep} \leq 0.0068$ eV/atom) the final aspect ratio is almost independent of energy. At higher deposition energies ($E_{\rm dep} \geq 0.068$ eV/atom), the nanoparticle aspect ratio increases over the first few picoseconds and eventually converges to the value of $\delta \approx 3$ at the end of simulations for each $E_{\rm dep}$. In contrast, a gradual increase of the final value of δ from about 1 to 2 is typical for the intermediate low-energy depositions (0.0068 eV/atom $< E_{\rm dep} \leq 0.034$ eV/atom).

As discussed above, the nanoparticle deposited in the "soft" regime remains in the solid phase in the course of deposition; this regime corresponds to a small increase of δ over time. For very low energies, the nanoparticle is deposited with minimal deformation (as observed in other MD simulations, e.g. [32]), with a partial wetting of the substrate due to the interplay of Na–Na and Na–substrate interatomic interactions. In the intermediate energy range the deposition is accompanied with plastic deformation, resulting in the progressive increase of aspect ratio with deposition energy, observed both experimentally and by simulations for other systems [21, 27, 30, 31]. When temperature of the nanoparticle exceeds its melting temperature, the nanoparticle experiences the melting phase transition and thus it becomes more susceptible to stress-induced deformation. This occurs at more energetic collisions when the nanoparticle wets the substrate and acquires the shape of an oblate spheroid, see Fig. 2(d-e). On this basis it is straightforward to explain the dependencies shown in Fig. 5(b), which describe the aspect ratio for the nanoparticle pre-equilibrated at 300 K. A liquid sodium drop deposited on MgO experiences strong deformation upon contacting the substrate. This behavior is characterized by a rapid increase of δ (i.e. flattening of the nanoparticle) within the first $5 - 10$ ps of the simulations. At larger time instances δ saturates at a constant value of about 3 when the nanoparticle reaches thermal equilibrium with the substrate. Note that the nanoparticles deposited at different values of $E_{\rm dep}$ have a similar shape as the aspect ratio asymptotically approaches a constant value $\delta \approx 3$.

The contact angle θ of a (macroscopic) liquid droplet on a planar surface is given by the Young equation as:

$$\gamma_{\rm SG} - \gamma_{\rm LS} - \gamma_{\rm LG} \cos\theta = 0 \ , \qquad (7)$$

where $\gamma_{\rm SG}$, $\gamma_{\rm LG}$ and $\gamma_{\rm LS}$ are, respectively, the interfacial energies between the solid and its gas, the liquid and its gas, as well as the liquid and the solid. In the temperature range considered in this study, $\gamma_{\rm SG} \approx 1.2$ J/m^2 [61] and $\gamma_{\rm LG} \approx 0.2$ J/m^2 [62]. From these values, we obtain from our simulations the value $\gamma_{\rm LS} \approx 1.1$ J/m^2 which, as far as we know, is not available in the literature. However, it should be noted that this is an approximate value valid for Na nanoparticles of 4 nm diameter on MgO, as it is known that interfacial energies for nanometer-sized droplets depend on their size [63].

To complete this analysis, Fig. 6 presents the comparison of the final aspect ratio and contact angle of deposited nanoparticles, which were initially equilibrated at two different temperatures, 77 K (blue circles) and 300 K (black squares). These parameters are evaluated in a broad deposition energy range below the nanoparticle fragmentation threshold. For each $E_{\rm dep}$, average values and standard deviations in time are calculated for the parts of the trajectories at which δ and θ oscillate around a constant value. Symbols represent the mean values while error bars correspond to a standard deviation.

Two different trends are clearly seen for different deposition temperatures. At 300 K (black squares) both the aspect ratio and the contact angle are practically con-

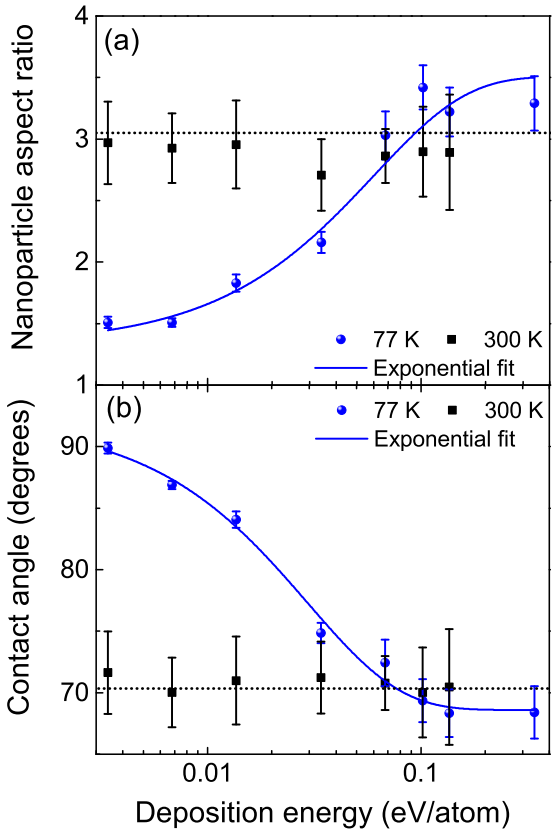

FIG. 6. The final aspect ratio (a) and contact angle (b) of the nanoparticle as functions of the deposition energy. Symbols denote time averages, while error bars represent standard deviations. Data for the deposition at 77 K are fitted with Eqs. (8) and (9).

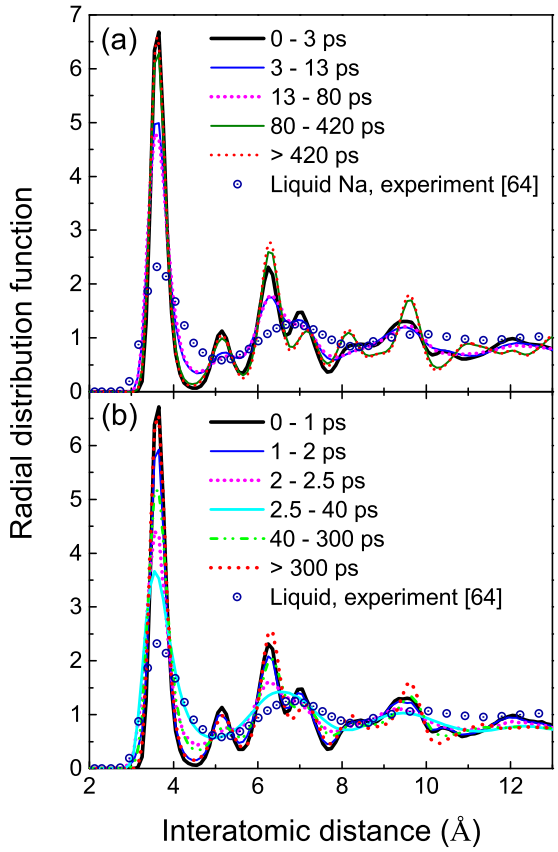

FIG. 7. Radial distribution function (RDF) for the Na_{1067} nanoparticle deposited at (a) 0.0068 eV/atom and (b) 0.068 eV/atom. Different curves describe the RDF evaluated over different time periods as indicated. These time periods are marked by dash-dotted vertical lines in Fig. 3(a,b).

stant within the studied energy range. Both parameters fluctuate around some characteristic values, $\delta \approx 3$ and $\theta \approx 70°$, which are indicated by horizontal dotted lines. For deposition at 77 K (blue circles), aspect ratio grows with $E_{\rm dep}$ while the contact angle decreases. The dependencies of δ and θ on $E_{\rm dep}$ have been fitted with the following exponential functions:

$$\delta = \delta_0 + \delta_1\, e^{\alpha\, E_{\rm dep}}\ , \qquad (8)$$

$$\theta = \theta_0 + \theta_1\, e^{-\gamma\, E_{\rm dep}}\ . \qquad (9)$$

Parameters of this fit are listed in Table II. At deposition energies larger than 0.068 eV/atom both aspect ratio and the contact angle for the nanoparticle deposited at 77 K approach the values obtained at 300 K as a consequence of the collision-induced melting phase transition above this energy. These results agree with the conclusions made above that the resulting shape of a liquid droplet deposited at 300 K depends very little on the deposition energy. In contrast, structure and contact angle for the nanoparticle deposited at the lower temperature strongly depend on $E_{\rm dep}$.

D. Collision-induced structural and phase transformations

Further insights into the change of internal structure of the deposited nanoparticle can be drawn from the analysis of the radial distribution function (RDF). Figure 7 shows RDFs for the nanoparticle equilibrated at 77 K and deposited at $E_{\rm dep} = 0.0068$ eV/atom (panel (a)) and $E_{\rm dep} = 0.068$ eV/atom (panel (b)). The plotted RDFs are averaged over different periods of time, which are marked by dashed vertical lines in Fig. 3(a,b). The RDFs for the deposited Na_{1067} nanoparticle are compared with the experimentally determined distribution for liquid sodium [64].

As shown in Fig. 7(a) main peaks in the RDFs remain from the initial stage of deposition (within the first 3 ps of simulation) up to the last stage when the nanoparticle has reached thermal equilibrium with the substrate (> 420 ps). Moreover, at all stages of the simulated trajectory the calculated RDFs differ from the one for liquid sodium (see open symbols). The melting phase transition and subsequent re-crystallization of the nanoparticle is

clearly seen by the variation of RDFs in Fig. 7(b). Temperature of the nanoparticle deposited at 0.068 eV/atom reaches the maximum value at about 2.5 ps and it remains higher than the melting temperature up to about 40 ps, see Fig. 3(b). In between these time instances the nanoparticle transforms into a liquid droplet as confirmed by the close similarity of the calculated RDF with the one for liquid sodium [64]. At larger time instances (the region of $40-300$ ps) the nanoparticle re-crystallizes and eventually reaches thermal equilibrium with the substrate at about 400 ps. Re-crystallization manifests itself in reappearance of peaks in the RDF, which resembles the RDF in the very beginning of the simulation.

IV. CONCLUSION

In this paper deposition of a nanometer-sized sodium nanoparticle, containing 1067 atoms, on a MgO substrate was studied by means of molecular dynamics simulations using the MBN Explorer and MBN Studio software packages. We focused on the broad deposition energy range of $0.0034 - 1.36$ eV/atom, which covers both the soft-landing and nanoparticle fragmentation regimes. Simulations were performed at two different temperatures, 77 K and 300 K, at which the nanoparticle is either in the solid state or it forms a liquid droplet.

A force field describing the interaction of sodium atoms with the MgO surface was developed and used in the simulations. The force field was validated via calculating adsorption energies of a single Na atom on different MgO sites. The presented results agreed with the results obtained previously in *ab initio* QM/MM simulations [29, 35, 37].

The process of nanoparticle deposition and subsequent relaxation on the surface has been studied in detail as a function of deposition energy. In particular, variation of the nanoparticle shape as a function of simulation time, its wetting properties, as well as the energy transfer between the nanoparticle and the substrate were analyzed on the timescale of up to several hundreds picoseconds. This study provides detailed insights into the dynamics of sodium nanoparticle deposition on MgO substrates which complement the information already gathered for small clusters from QM/MM simulations and which may be useful for experimental studies. A similar analysis for other metallic aggregates deposited onto experimentally relevant oxide surfaces might reveal atomistic-level insights into the structure and shape of the deposited metal systems, which might be useful for technological applications.

ACKNOWLEDGEMENTS

This work was supported in part by Deutsche Forschungsgemeinschaft (Project no. 415716638); by the European Union's Horizon 2020 research and innovation programme – the Radio-NP project (GA 794733) within the H2020-MSCA-IF-2017 call and the RADON project (GA 872494) within the H2020-MSCA-RISE-2019 call; by the Spanish Ministerio de Ciencia e Innovación and the European Regional Development Fund (Project no. PGC2018-096788-B-I00); by the Fundación Séneca – Agencia de Ciencia y Tecnología de la Región de Murcia (Project No. 19907/GERM/15); and by the Conselleria d'Educació, Investigació, Cultura i Esport de la Generalitat Valenciana (Project no. AICO/2019/070). PdV gratefully acknowledges the Alexander von Humboldt Foundation/Stiftung and the Spanish Ministerio de Ciencia e Innovación for their financial support by means of, respectively, Humboldt (1197139) and Juan de la Cierva (FJCI-2017-32233) postdoctoral fellowships. The possibility to perform computer simulations at Goethe-HLR cluster of the Frankfurt Center for Scientific Computing and the Scientific Computing Service of the University of Murcia is gratefully acknowledged.

[1] W. A. de Heer, Rev. Mod. Phys. **65**, 611 (1993).
[2] H. Haberland, ed., *Clusters of Atoms and Molecules. Theory, Experiment, and Clusters of Atoms* (Springer-Verlag, Berlin Heidelberg, 1994).
[3] U. Kreibig and M. Vollmer, *Optical Properties of Metal Clusters* (Springer-Verlag, Berlin Heidelberg, 1995).
[4] K.-H. Meiwes-Broer, ed., *Metal Clusters at Surfaces. Structure, Quantum Properties, Physical Chemistry* (Springer-Verlag, Berlin Heidelberg, 2000).
[5] J.-P. Connerade and A. Solov'yov, eds., *Latest Advances in Atomic Cluster Collisions: Structure and Dynamics from the Nuclear to the Biological Scale* (Imperial College Press, London, 2008).
[6] P. M. Dinh, P.-G. Reinhard, and E. Suraud, *An Introduction to Cluster Science* (Wiley-VCH, Berlin, 2013).
[7] F. Calvo, Phys. Chem. Chem. Phys. **17**, 27922 (2015).
[8] S. T. Bromley and S. M. Woodley, eds., *Computational Modelling of Nanoparticles, Frontiers of Nanoscience vol. 12* (Elsevier, 2018).
[9] D. B. Janes, M. Batistuta, S. Datta, M. R. Melloch, R. P. Andres, J. Liu, N. P. Chen, T. Lee, R. Reifenberger, E. H. Chen, and J. M. Woodall, Superlattices Microstruct. **27**, 555 (2000).
[10] L. Sun, H. Lin, K. L. Kohlstedt, G. C. Schatz, and C. A. Mirkin, Proc. Natl. Acad. Sci. U.S.A. **115**, 7242 (2018).
[11] U. Heiz and U. Landman, eds., *Nanocatalysis* (Springer-Verlag, Berlin Heidelberg, 2007).
[12] X. Han, K. Xu, O. Taratula, and K. Farsad, Nanoscale **11**, 799 (2019).
[13] K. Haume, S. Rosa, S. Grellet, M. A. Śmiałek, K. T. Butterworth, A. V. Solov'yov, K. M. Prise, J. Golding, and N. J. Mason, Cancer Nanotechnol. **7**, 8 (2016).
[14] A. V. Verkhovtsev, A. V. Korol, and A. V. Solov'yov, Phys. Rev. Lett. **114**, 063401 (2015).

[15] Y. Liu, P. Zhang, F. Li, X. Jin, J. Li, W. Chen, and Q. Li, Theranostics **8**, 1824 (2018).

[16] C. L. Cleveland and U. Landman, Science **257**, 355 (1992).

[17] H. Haberland, Z. Insepov, and M. Moseler, Phys. Rev. B **51**, 11061 (1995).

[18] Z. Insepov and I. Yamada, Nucl. Instrum. Meth. B **112**, 16 (1996).

[19] Y. Yamaguchi and J. Gspann, Eur. Phys. J. D **8**, 103 (2001).

[20] Y. Yamaguchi and J. Gspann, Phys. Rev. B **66**, 155408 (2002).

[21] V. N. Popok, I. Barke, E. E. Campbell, and K. H. Meiwes-Broer, Surf. Sci. Rep. **66**, 347 (2011).

[22] P. Milani and M. Sowwan, eds., *Cluster Beam Deposition of Functional Nanomaterials and Devices, Frontiers of Nanoscience vol. 15* (Elsevier, 2020).

[23] D. N. Poenaru, R. A. Gherghescu, A. V. Solov'yov, and W. Greiner, EPL (Europhys Lett.) **79**, 63001 (2007).

[24] D. N. Poenaru, R. A. Gherghescu, I. H. Plonski, A. V. Solov'yov, and W. Greiner, Eur. Phys. J. D **47**, 379 (2008).

[25] H. Häkkinen, Adv. Phys. X **1**, 467 (2016).

[26] H. Hövel, B. Grimm, M. Pollmann, and B. Reihl, Phys. Rev. Lett. **81**, 4608 (1998).

[27] A. V. Verkhovtsev, Y. Erofeev, and A. V. Solov'yov, Eur. Phys. J. D **74**, 205 (2020).

[28] H. Häkkinen and M. Manninen, J. Chem. Phys. **105**, 10565 (1996).

[29] M. Bär, *Non-Linear Dynamics of Metal Clusters on Insulating Substrates*, PhD Thesis, Friedrich-Alexander-Universität Erlangen-Nürnberg (2008).

[30] L. Bardotti, B. Prével, P. Mélinon, A. Perez, Q. Hou, and M. Hou, Phys. Rev. B **62**, 2835 (2000).

[31] Q. Hou, M. Hou, L. Bardotti, B. Prével, P. Mélinon, and A. Perez, Phys. Rev. B **62**, 2825 (2000).

[32] J. C. Jiménez-Sáez, A. M. Pérez-Martín, and J. J. Jiménez-Rodríguez, Nucl. Instrum. Meth. B **249**, 816 (2006).

[33] U. Landman, Proc. Natl. Acad. Sci. U.S.A. **102**, 6671 (2005).

[34] Z. Insepov, *Cluster-Ion Solid Interactions. Theory, Simulation, and Experiment* (CRC Press, Boca Raton, 2016).

[35] P. M. Dinh, P. G. Reinhard, and E. Suraud, Phys. Rep. **485**, 43 (2010).

[36] M. Bär, L. V. Moskaleva, M. Winkler, P. G. Reinhard, N. Rösch, and E. Suraud, Eur. Phys. J. D **45**, 507 (2007).

[37] M. Bär, P. M. Dinh, L. V. Moskaleva, P. G. Reinhard, N. Rösch, and E. Suraud, Phys. Rev. B **80**, 195404 (2009).

[38] C. R. Henry, Surf. Sci. Rep. **31**, 231 (1998).

[39] G. Barcaro, A. Fortunelli, F. Nita, and R. Ferrando, Phys. Rev. Lett. **95**, 246103 (2005).

[40] G. Barcaro and A. Fortunelli, J. Chem. Theory Comput. **1**, 972 (2005).

[41] D. Paradiso and J. Z. Larese, J. Phys. Chem. C **124**, 14564 (2020).

[42] F. Buendía, A. T. Anzaldo, C. Vital, and M. R. Beltrán, J. Chem. Phys. **152**, 024303 (2020).

[43] T. T. Magkoev, G. S. Grigorkina, V. B. Zaalishvili, O. G. Burdzieva, E. N. Kozyrev, G. E. Tuaev, and K. Fukutani, Rus. J. Phys. Chem. A **94**, 401 (2020).

[44] S. Nigam and C. Majumder, Appl. Surf. Sci. **506**, 144963 (2020).

[45] R. S. Averback and M. Ghaly, Nucl. Instrum. Meth. B **90**, 191 (1994).

[46] S. J. Carroll, P. D. Nellist, R. E. Palmer, S. Hobday, and R. Smith, Phys. Rev. Lett. **84**, 2654 (2000).

[47] T. J. Colla, R. Aderjan, R. Kissel, and H. M. Urbassek, Phys. Rev. B **62**, 8487 (2000).

[48] M. Moseler, O. Rattunde, J. Nordiek, and H. Haberland, Nucl. Instrum. Meth. B **164**, 522 (2000).

[49] I. A. Solov'yov, A. V. Korol, and A. V. Solov'yov, *Multiscale Modelling of Complex Molecular Structure and Dynamics with MBN Explorer* (Springer International Publishing, 2017).

[50] T. P. Martin, U. Näher, H. Schaber, and U. Zimmermann, J. Chem. Phys. **100**, 2322 (1994).

[51] I. A. Solov'yov, A. V. Yakubovich, P. V. Nikolaev, I. Volkovets, and A. V. Solov'yov, J. Comput. Chem. **33**, 2412 (2012).

[52] G. B. Sushko, I. A. Solov'yov, and A. V. Solov'yov, J. Mol. Graph. Model. **88**, 247 (2019).

[53] A. M. Dongare, D. D. Hass, and L. V. Zhigilei, Clusters and Nano-Assemblies: Physical and Biological Systems: Richmond, Virginia, U.S.A., 10-13 November, 2003 , 329 (2005).

[54] M. Moseler, J. Nordiek, and H. Haberland, Phys. Rev. B **56**, 15439 (1997).

[55] Y. Li, E. Blaisten-Barojas, and D. A. Papaconstantopoulos, Chem. Phys. Lett. **268**, 331 (1997).

[56] T. Ellaby, J. Aarons, A. Varambhia, L. Jones, P. Nellist, D. Ozkaya, M. Sarwar, D. Thompsett, and C.-K. Skylaris, J. Phys.: Condens. Matter **30**, 155301 (2018).

[57] I. A. Solov'yov, A. V. Solov'yov, W. Greiner, A. Koshelev, and A. Shutovich, Phys. Rev. Lett. **90**, 053401 (2003).

[58] H. Haberland, T. Hippler, J. Donges, O. Kostko, M. Schmidt, and B. von Issendorff, Phys. Rev. Lett. **94**, 035701 (2005).

[59] N. Giovambattista, P. G. Debenedetti, and P. J. Rossky, J. Phys. Chem. B **111**, 9581 (2007).

[60] J. Škvára, J. Škvor, and I. Nezbeda, Molec. Simul. **44**, 190 (2018).

[61] G. Jura and C. W. Garland, J. Am. Chem. Soc. **74**, 6033 (1952).

[62] B. D. Jordan and J. E. Lane, Aust. J. Chem. **18**, 1711 (1965).

[63] J. Murai, T. Marukawa, T. Mima, S. Arai, K. Sasaki, and H. Saka, J. Mater. Sci. **41**, 2723 (2006).

[64] R. D. Murphy and M. L. Klein, Phys. Rev. A **8**, 2640 (1973).